Available online at www.sciencedirect.com

jmr&t Journal of Materials Research and Technology

www.jmrt.com.br

Original Article

The effects of Cr addition on microstructure, hardness and tensile properties of as-cast Al–3.8wt.%Cu–(Cr) alloys

Thiago M. Ribeiro[a], *Eduardo Catellan*[a], *Amauri Garcia*[b], *Carlos A. dos Santos*[a,*]

[a] *Pontifícia Universidade Católica do Rio Grande do Sul – PUCRS, School of Technology, Av. Ipiranga, 6681, 90.619-900, Porto Alegre, RS, Brazil*

[b] *University of Campinas – UNICAMP, Department of Manufacturing and Materials Engineering, 13083-860, Campinas, SP, Brazil*

ARTICLE INFO

Article history:
Received 7 August 2019
Accepted 18 April 2020
Available online 12 May 2020

Keywords:
Al–Cu–Cr Alloy
Solidification
Microstructure
Hardness
Tensile strength

ABSTRACT

An investigation is made on the effects of Cr addition (0.25 and 0.50 wt%) on the solidification evolution, microstructure formation, hardness and tensile properties of Al–3.8Cu–(Cr) alloys. Solidification experiments were carried out in a vertical furnace using a metallic mold cooled from the bottom, thus permitting solidified ingots under transient heat flow conditions to be obtained. The solidification system was instrumented with thermocouples at positions along the length of the ingot to permit the solidification cooling rate to be determined from bottom to top of the ingots. The ingots were transversally and longitudinally sectioned to extract specimens for metallographic analyze, hardness and tensile tests. The macrostructures are shown to be entirely columnar along the length of the Al–3.8Cu and Al–3.8Cu–0.25Cr alloys ingots, whereas the Al–3.8Cu–0.50Cr alloy is shown to have a columnar-to-equiaxed transition close to the top. For any alloy ingot examined, the Al-rich matrix is characterized by a cellular morphology for high cooling rates followed by cellular/dendritic transitions with the decrease in cooling rate. The addition of Cr to the Al–3.8Cu alloy promoted the formation of $Al_{23}CuFe$ and $Al_7CuCrFe$ phases precipitated in the matrix and eutectic mixture, preventing formation of isolated Al–Fe intermetallic compounds. Hardness and tensile strength increased with increasing alloy Cr content, with highest values of both properties associated with the Al–3.8Cu–0.50Cr alloy ingot. Experimental equations correlating hardness/tensile strength and cellular spacing are proposed. These equations were coupled to the theoretical Hunt–Lu model to estimate hardness and ultimate tensile strength as a function of the cellular spacing.

1. Introduction

Al–Cu alloys are widely used in engineering applications due to their enhanced physical–chemical properties, such as light weight, high mechanical strength and thermal/electrical conductivity, corrosion resistance and manufacturing feasibility. These alloys were developed in the early 1900s, found in the as-cast and wrought conditions. They were the first precipitation-hardening heat-treatable aluminum alloy with Cu content ranging from 1.0 to 5.65 wt.% [1]. In general, the microstructure is characterized by an α-Al matrix containing $CuAl_2$ intermetallic particles, θ phase, precipitated in the matrix. When other alloying elements as Mg, Si, Zn, Fe and

* *Corresponding author.*
E-mail: carlos.santos@pucrs.br (C.A. dos Santos).

https://doi.org/10.1016/j.jmrt.2020.04.054

others are added, specific characteristics are improved, e.g., toughness, castability and workability at elevated temperatures, by changing microstructure, precipitation-hardening and interaction between matrix/secondary phases during plastic deformation [2–6].

$CuAl_2$ intermetallic particles can be found precipitated along the grain boundaries, interdendritic regions and/or inside the grains, depending on the alloy Cu concentration and solidification conditions [7,8]. In the presence of Fe, acicular particles of AlFe and/or AlCuFe can be formed, reducing, consequently, mechanical and corrosion resistances [9,10] even though Fe content is lower than 0.1 wt%. When Cr is added to the alloys, complex AlFeCr particles can appear, and the possibility to find needle-like AlFe particles is minimized. Recently, studies have been carried out to investigate the effects of Cr addition on the microstructure formation and the resultant mechanical properties of Al–Cu alloys. Cr has low solubility in the α-Al matrix, showing a tendency to form intermetallic precipitates with Al, Cu and other elements [11]. When the Cr content is increased and the presence of Fe is higher, quasicrystal structures with specific characteristics as high mechanical properties (tensile strength and hardness) and low friction coefficient are formed. The most studied alloys are in the range of $Al_{65–69}Cu_{20–23}Fe_{10–12}Cr_{5–16}$ (at.%) with high Cu, Fe and Cr contents, as reported by Sugiyama et al. [12]; Sviridova et al. [13]; Fu et al. [14] and Salimon et al. [15]. These investigations focused on the quasicrystal structure formation (Al–Cr, Al–Fe, Al–Cu–Cr and Al–Cu–Fe) due to processing procedures as conventional solidification, mechanical alloying and selective laser melting.

However, the literature still has scarce information concerning the effect of low Cr content on the relationship between solidification conditions, microstructure evolution and mechanical properties of hypoeutectic Al–Cu alloys. In addition, both the understanding of solute redistribution during solidification and the cellular/dendritic array formation under unsteady–state solidification conditions of Al–Cu–Cr alloys using theoretical/experimental models are limited. Most models were developed to predict cellular and/or dendritic growth of binary alloys and few have considered transient heat flow conditions. Among these models, the numerical model proposed by Hunt and Lu [16] for non-steady-state cellular/dendritic array growth seems to be the most suitable, due to its physics considerations. Heat flow and solute transport in the liquid depends on time and the solid/liquid interface surface energy is considered. The expression proposed to estimate the cellular spacing is given by:

$$\lambda_c = 8.18 k_0^{-0.745} \left(\frac{\Gamma}{\Delta T_0}\right)^{0.41} D^{0.59} V_L^{-0.59} \quad (1)$$

where λ_c is the cellular spacing (μm), k_0 the distribution coefficient (C_s/C_L), Γ the Gibbs Thomson coefficient (m K), ΔT_0 the difference between the *Liquidus* and *Solidus* equilibrium temperatures, D the liquid solute diffusivity (m^2/s) and V_L the solidification growth rate (m/s). As λ_c refers to the cell radius, the results must be multiplied by 2 for comparison with measured diameter spacings. Hunt and Lu [16] evaluated the lower and upper limits of the spacings within which an array can be stable, and proposed that the upper limit should be twice the lower one. According to the authors, this expression can be applied for predicting cellular spacing in a wide range of growth conditions (under low and high velocities).

The aim of this work is to investigate the influence of Cr addition (0.25 and 0.50 wt.%) to the Al–3.8 wt.%Cu alloy on solidification conditions, microstructure evolution and hardness/tensile properties, establishing correlations between solidification parameters, microstructural features and mechanical properties based on experimental data and the cellular growth model proposed by Hunt and Lu [16].

2. Materials and methods

The Al–3.8Cu (wt.%) base alloy was prepared using pure aluminum (99.8Al–0.091Fe–0.046Si–0.063 balance) and electrolytic copper (>99.99% purity), melted at 750 °C during 1/2 hour in a silicon carbide crucible using an electric resistive pit furnace and poured into chill molds. Al–Cu–Cr alloys were prepared by adding pure Cr (99.7Cr–0.10Fe_{max}–0.10Si_{max}–0.1 balance) in small blocks into the Al–Cu molten alloy at 900 °C. The alloys were mechanically stirred for 3 h (5 min in intervals of 15 min) using a stainless-steel bar coated with boron nitride. The temperature was then lowered to 750 °C and the alloys poured into chill molds. Chemical compositions were analyzed by optical emission spectrometry (OES). Average results of six measurements for each alloy are shown in Table 1. As observed, all alloys presented chemical compositions closer to the nominal compositions, with exception of the Fe content that was increased due to its presence in the raw materials and the possible contamination from the contact between molten metal and accessories used during melting.

Fig. 1a–c present the Al–3.8Cu–xCr, Al–3.8Cu–xFe and Al–0.5Cr–xFe partial pseudo-binary phase diagrams simulated by the Thermo-Calc software, in which the vertical dashed lines (Fig. 1a) indicate the nominal Cr compositions analyzed in this work. According to the diagram, the solidification temperature ranges are $T_L = 652$ °C (*Liquidus* temperature) and $T_S = 575$ °C (*Solidus* temperature) for the Al–3.8Cu–0.25Cr alloy and $T_L = 679$ °C and $T_S = 573$ °C for the Al–3.8Cu–0.50Cr alloy, whereas the Al–3.8Cu base alloy presents values of $T_L = 645$ °C and $T_S = 548$ °C [1]. According to the calculated Al–3.8Cu–xCr pseudo-binary phase diagram, the solidification path of the alloys containing 0.25 and 0.50Cr is: $L \rightarrow L + Al_7Cr \rightarrow L + Al_7Cr + \alpha\text{-}Al \rightarrow Al_7Cr + \alpha\text{-}Al \rightarrow Al_7Cr + \alpha\text{-}Al + \theta\text{-}CuAl_2$. When analyzing the Al–3.8Cu–xFe diagram, the Al_7Cu_2Fe phase can be formed if the Fe content is higher than 0.02%, and the $Al_{13}Fe_4$ precipitates at higher temperatures only if the Fe content is higher than 0.13%, whereas in the Al–0.50Cr–xFe phase diagram the $Al_{13}Fe_4$ phase is present when the Fe concentration is higher than 0.2%. These observations agree with those reported in the literature for Al–Cu–(Cr–Fe) alloys with different Cr and Fe contents [11,15].

The alloys were remelted in a cylindrical (120 mm internal-diameter, 250 mm high) SAE 1020 steel mold using a vertical tubular resistive furnace. The metal was monitored by 1.6 mm diameter type-K thermocouples positioned at 6, 12, 18, 24, 30

Table 1 – Chemical composition of the alloys.

Alloy	Elements (wt%)								
	Cu	Cr	Si	Fe	Ni	Ti	Mn	Mg	Al
Al–3.8Cu	3.81	0.007	0.061	0.137	0.002	0.002	0.009	0.001	Balance
Al–3.8Cu–0.25Cr	3.79	0.256	0.059	0.139	0.004	0.001	0.001	0.001	Balance
Al–3.8Cu–0.50Cr	3.85	0.488	0.092	0.177	0.008	0.008	0.010	0.002	Balance

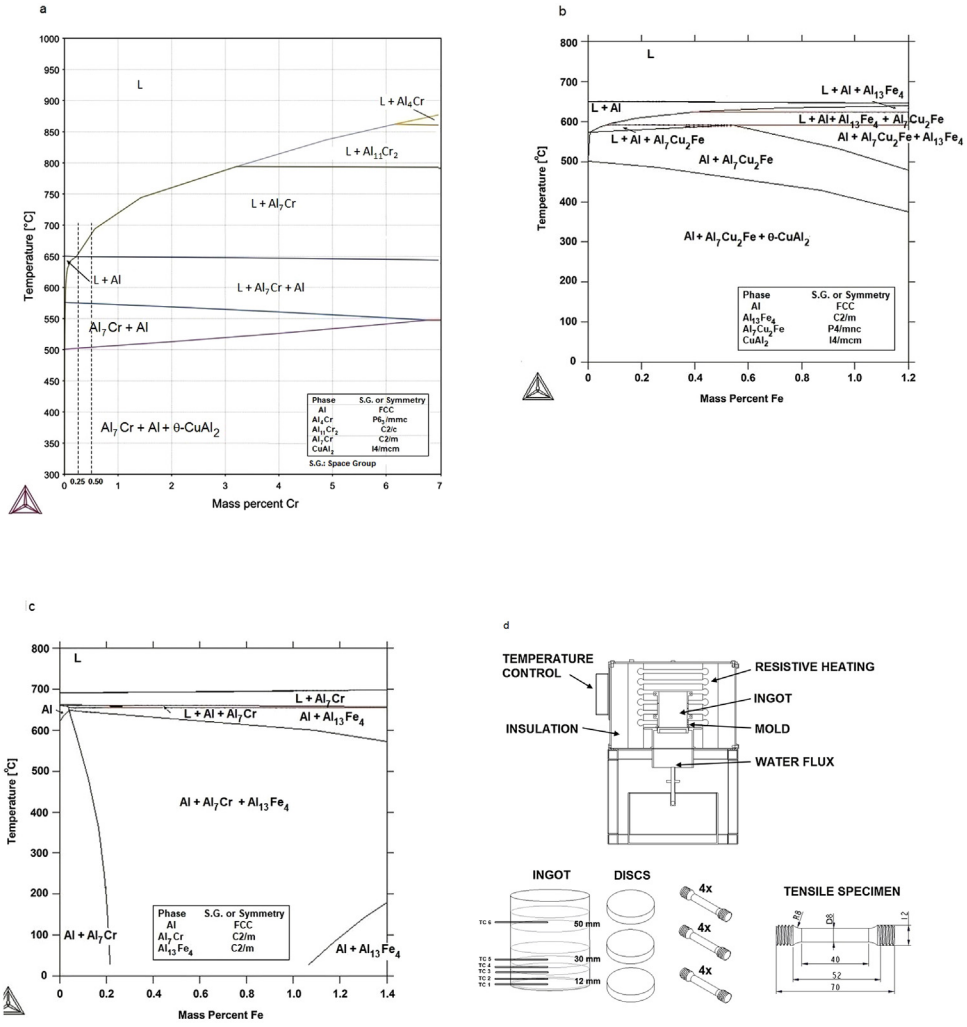

Fig. 1 – (a) Al–3.8Cu–*x*Cr, (b) Al–3.8Cu–*x*Fe and (c) Al–0.50Cu–*x*Fe partial pseudo-binary phase diagrams (Thermo-Calc), (d) solidification apparatus and samples/specimens extracted from the directionally solidified ingots.

and 50 mm from the bottom of the water-cooled mold. When the molten metal achieved the desired temperature (~720 °C), the furnace was powered-off and a water-flux (4 l/min) cooled the mold bottom, allowing the onset of upward directional solidification under transient heat flow conditions. The thermal profiles acquired by each thermocouple along the length of the alloy ingots were used to determine the evolution of cooling rates during solidification from bottom to top of the ingot. Two identical 2 kg ingots were obtained for each examined alloy.

Longitudinal samples were extracted from the alloy ingots for metallographic analyzes using standard procedures [17,18]. Aqua regia solution (2:6:1 HNO_3–HCl–HF) was used for revealing macrostructures and an electro-polishing solution (8:1.4:0.6 ethanol–distilled water–perchloric acid – 20 V/20 s) for microstructures. Analyzes were performed by optical (OM) and scanning electron microscopies (FEG-SEM), energy dispersive X-ray spectroscopy (EDS), X-ray diffraction (Cu-$K\alpha_1$ radiation, 2θ scanning range: 10–100°, 40 kV, 30 mA) and Vickers microhardness [19]. Specimens were prepared for mechanical testing (hardness and tensile tests) as recommended by standard test methods [20,21]. Fig. 1d shows a schematic representation of the solidification apparatus and samples/specimens extracted from the alloys' ingots.

3. Results and discussion

3.1. Cooling curves, solidification cooling rate and macrostructure

Fig. 2 shows the cooling curves acquired during upward directional solidification of each alloy ingot. Equilibrium *Liquidus* temperatures (T_L) of each alloy are displayed on the graphs as well as the corresponding longitudinal macrostructures. Since solidification occurs at higher cooling rates for positions near the cooled bottom of the ingots, the change in slope in the cooling curve due to the onset of solidification (at the liquidus temperatures) is imperceptible. The liquidus temperatures were determined from the Al–Cu equilibrium phase diagram [1] for the Al–3.8Cu alloy and from the Al–Cu–Cr pseudo-binary phase diagram showed in Fig. 1a for the Al–Cu–Cr alloys. First derivative (with respect to time) of the cooling curves were used to support the determination of the start of solidification. Analyzing the cooling curves, the beginning of solidification occurred at higher temperatures for the alloys containing Cr, when compared to the Al–3.8Cu base alloy (Fig. 2a), since the addition of Cr increased T_L from 645 °C in the Al–3.8Cu to 652 °C and 679 °C in the Al–3.8Cu–0.25Cr (Fig. 2b) and Al–3.8Cu–0.50Cr alloys (Fig. 2c), respectively. For positions close to the bottom of the mold the cooling curves are associated with higher heat extraction rates, which decrease progressively toward the top of the ingots. Furthermore, the observed inflections in the graphs for positions closer to the mold surface are due to the end of solidification at these positions. The solidified layer has a higher thermal resistance to heat extraction due to its lower thermal conductivity as compared to that of the liquid metal. Consequently, when the first thermocouple (TC1) reaches approximately 550 °C, the non-equilibrium eutectic is formed and the latent heat is released. This reflects the temperature evolution of the cooling curve that has its slope changed moving upwards. The Al–3.8Cu and Al–3.8Cu–0.25Cr macrostructures are predominantly columnar along the entire ingots lengths with grains growing vertically aligned to the heat flux direction. The Al–3.8Cu–0.50Cr alloy ingot showed a columnar-to-equiaxed transition (CET) approximately at 60 mm from the ingot bottom, as well as smaller average columnar-grain diameter when compared to the other alloys. Based on the approach by Siqueira et al. [22] for Al–Cu and Sn–Pb alloys unidirectionally solidified, the columnar growth prevails for cooling rates higher than a critical value. In the case of Al–Cu alloys, the proposed value was about 0.2 °C/s. This criterion seems appropriate to predict the CET for binary Al–Cu alloys. However, the Al–3.8Cu–0.50Cr alloy ingot has a CET associated with a quite higher cooling rate (about 0.7 °C/s), as can be observed in Fig. 3.

Using the experimental thermal profiles, the time (t_L) associated with the passage of the *Liquidus* isotherm by each thermocouple position (P_L) has been determined and plotted in Fig. 3a. It can be seen that the velocity of displacement of the *Liquidus* isotherm increased with the increase in the alloy Cr content. This may be attributed to the influence of Cr on the solidification temperature ranges. The derivative of the function $P_L = f(t_L)$ with respect to time (t) gave values for tip growth rate ($V_L = dP_L/dt$), as shown in Fig. 3b. The temperature gradient in the melt ahead the solidification interface is presented in Fig. 3c. The cooling rate ($\dot{T} = dT/dt$) along the length of each alloy ingot was calculated by deriving the temperature (T) with respect to time (t), immediately after the passage of the *Liquidus* isotherm by each thermocouple, as depicted in Fig. 3d as a function of the distance from the bottom of the ingots (P). The effect of the alloys Cr content is also reflected on the tip growth and cooling rates, which gradually rise as the alloy Cr content is increased. Comparing the curves, the tip growth rate and cooling rate profiles of the Al–Cu–Cr alloys are higher than that of the Al–Cu alloy, particularly at positions near the bottom of the alloys ingots. An opposite behavior was observed associated with the liquid thermal gradient (Fig. 3c) for the Al–Cu–Cr alloys, which decreases with the increase in the alloy Cr content. However, the Al–3.8Cu–0.50Cr alloy showed higher liquid temperature gradient values at those positions near the top of the ingot (60 mm) when compared to the other alloys, clearing up the columnar-equiaxed transition observed in Fig. 2c.

Average chemical composition at those positions corresponding to the thermocouple's locations are shown in Table 2 for each alloy ingot. As noted, no evidence of macrosegregation was detected in the Cu, Cr and Fe profiles, and the nominal composition deviation was observed to be irrelevant for all alloying elements according to the standard deviation (SD) presented for each element.

3.2. Microstructures, cellular growth and cellular/dendritic transition

Longitudinal microstructures of the directionally solidified ingots are presented in Fig. 4. For the Al–3.8Cu alloy, a completely cellular microstructure can be observed at positions close to the ingot bottom (Fig. 4a). The cellular-to-dendritic transition was observed to occur at 50 mm from the metal/mold interface under a cooling rate of 0.53 °C/s. For the Cr-containing alloys, the cellular-to-dendritic transition took place at approximately 30 mm, under cooling rates of 0.92 °C/s and 1.18 °C/s for the 0.25Cr (Fig. 4b) and 0.50Cr (Fig. 4c) alloys, respectively. As reported by Rocha et al. [23–25] referring to Sn–Pb alloys, cellular structures prevail when a factor given by $\eta = (G_L/V_L)\cdot(1/C_0)$ is greater than 1.0, dendritic structures are stable for $\eta < 0.7$, and the cellular/dendritic transition occurs in the range between $0.7 < \eta < 1.0$. (G_L is the liquid thermal gradient, V_L the solidification growth rate and C_0 the solute concentration). In the present investigation, the following values were determined for the cellular/dendritic transition factor: $\eta = 1.67$ (for the Al–3.8Cu alloy), $\eta = 1.53$ (for the Al–3.8Cu–0.25Cr alloy), and $\eta = 1.09$ (for the Al–3.8Cu–0.50Cr alloy). These values are different from those found by Rocha et al. [23–25], suggesting that the cellular/dendritic transition of the investigated ternary Al–Cu–Cr alloys should occur in the range $1.0 < \eta < 1.5$.

The cellular spacings (λ_c) were correlated to the solidification cooling rates during solidification permitting to establish interrelations between representative microstructure length scale and solidification thermal parameter, as shown in Fig. 5. The points are average values of about 20 measurements for each position. An experimental growth law for λ_c as a function of the cooling rate ($\dot{T}$) has been derived in Fig. 5. A single

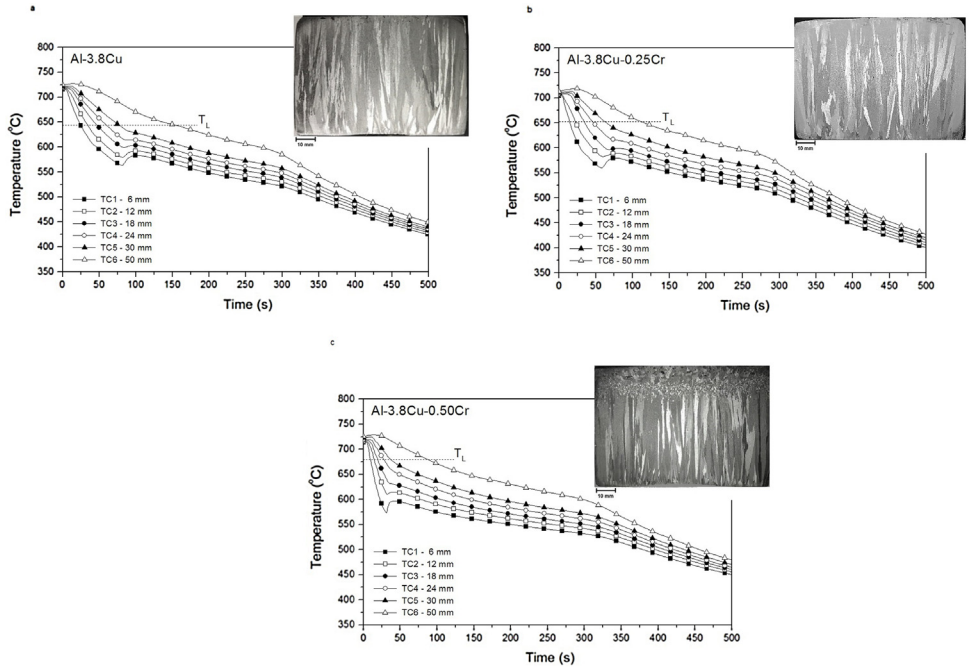

Fig. 2 – Thermal profiles and longitudinal macrostructures of: (a) Al–3.8Cu, (b) Al–3.8Cu–0.25Cr, (c) Al–3.8Cu–0.50Cr alloys ingots. *TC: thermocouple*.

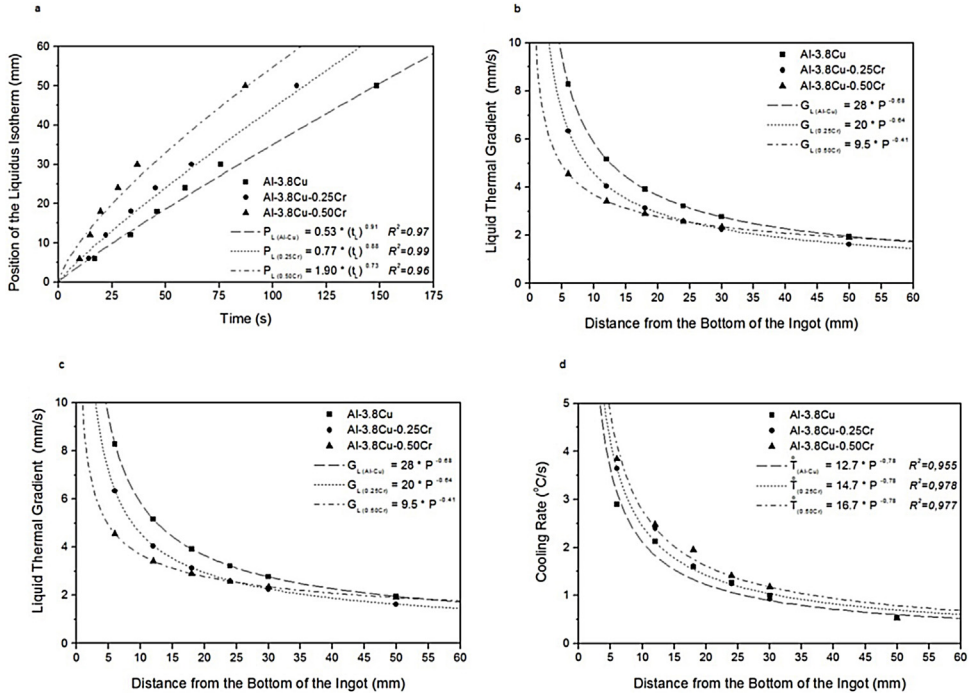

Fig. 3 – (a) Evolution of *Liquidus* isotherm over time along the length of the Al–3.8Cu, Al–3.8Cu–0.25Cr and Al–3.8Cu–0.50Cr alloys ingots, (b) tip growth rate, (c) liquid thermal gradient, and (d) cooling rate profiles along the length of the ingots, R^2: coefficient of determination.

power function equation with a −1/3 exponent represents the variation of λ_c for all examined alloys. The Hunt–Lu model (Eq. (1)) was used for comparison with experimental λ_c data, considering the thermophysical properties of the Al–3.8Cu alloy ($\Gamma \equiv 15.40 \times 10^{-8}$ m K, $k_0 = 0.17$, $D = 3.50 \times 10^{-9}$ m^2/s) [26–28]. It is worth noting that thermophysical properties of Al–Cu–Cr alloys are scarce in the literature. Since the present alloys Cr contents are quite low, the same thermophysical properties of the Al–3.8Cu alloy have been adopted in the calculations performed for the Cr-containing alloys. The solidification interval

Table 2 – Average chemical composition of the alloys at positions corresponding to the thermocouple's locations along the length of the directionally solidified ingots.

	Al–3.8Cu		Al–3.8Cu–0.25Cr			Al–3.8Cu–0.50Cr		
	Cu	Fe	Cu	Cr	Fe	Cu	Cr	Fe
TC1	3.79	0.141	3.91	0.246	0.156	3.93	0.491	0.168
TC2	3.81	0.146	3.82	0.248	0.152	3.82	0.491	0.162
TC3	3.81	0.140	3.88	0.247	0.156	3.81	0.490	0.163
TC4	3.85	0.146	3.83	0.248	0.153	3.81	0.491	0.162
TC5	3.86	0.147	3.80	0.248	0.152	3.99	0.495	0.165
TC6	3.81	0.138	3.76	0.248	0.148	3.86	0.494	0.163
SD	0.027	0.004	0.054	0.001	0.003	0.075	0.002	0.002

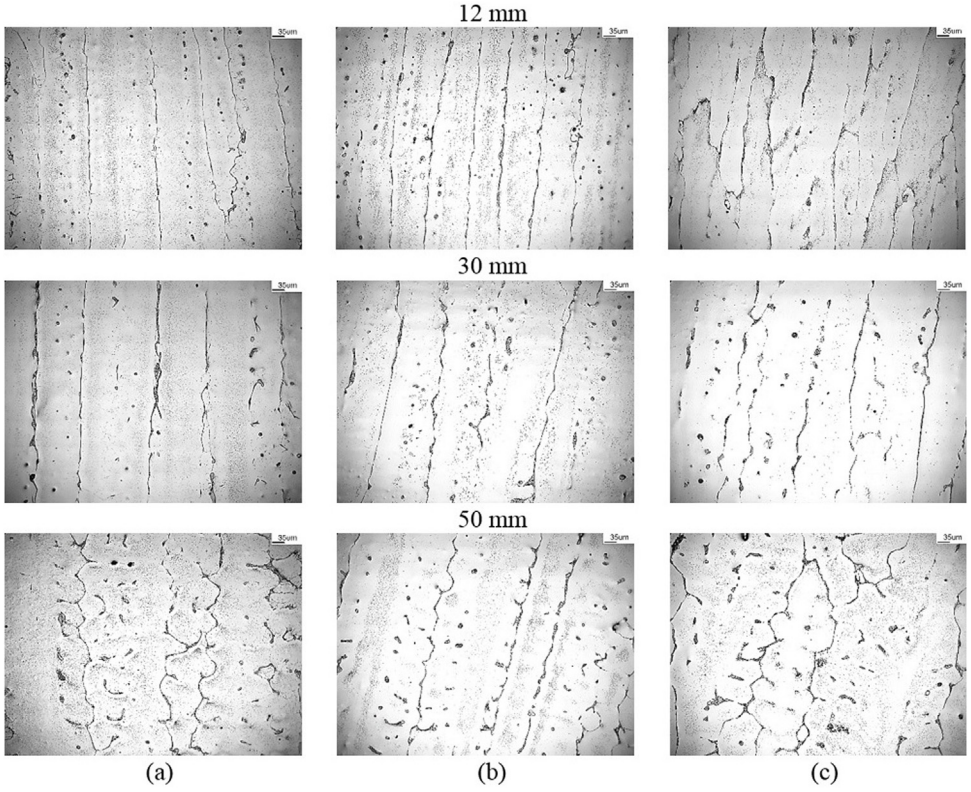

Fig. 4 – Microstructures of longitudinal sections along the length of: (a) Al–3.8Cu, (b) Al–3.8Cu–0.25Cr, (c) Al–3.8Cu–0.50Cr alloys ingots.

(ΔT_0) for each alloy was taken from the Al–Cu–Cr pseudo-binary phase diagram, and the adopted values are presented in Section 2. A good agreement can be observed between the experimental and theoretical results of Al–3.8Cu and Al–3.8Cu–0.25Cr alloys. With the increase in the alloy Cr content, the predictions furnished by the Hunt–Lu model move away from the measured values probably due to the inaccuracy of the adopted thermophysical properties for the 0.5Cr ternary alloy.

Figs. 6 and 7 show SEM images of Al–Cu–Cr alloys. For the 0.25Cr alloy (Fig. 6a), EDS analyzes confirmed an α-Al matrix with Cu in solid solution (EDS 1) and a eutectic mixture of $CuAl_2$ (EDS 2) and α-Al (EDS 3). The occurrence of irregular AlCuCrFe particles in the eutectic, inside and outside the boundaries, was also observed, as shown in Fig. 6b and c. Despite the phase equilibrium diagrams of Fig. 1a and b, which predict the presence of α-Al, $CuAl_2$ (θ) and Al_7Cr phases at low temperatures, the Al_7Cr phase is undetected as a consequence of the non-equilibrium solidification conditions of the present experiments, restricting the diffusion of Cr into the α-Al matrix, which remained segregated in the liquid phase and prone to combine with AlCuFe compounds, as predicted by the phase diagram of Fig. 1c. Moreover, AlFeCr and AlCuFeCr precipitates seem to act as substrates to nucleation of the eutectic mixture, as observed in Fig. 6b and c. This agrees with the results reported by Liu et al. [29] for an Al–5Fe alloy with Cr additions (1%, 2% and 3%). According to the authors, a small Cr addition increases both the cooling rate and compositional undercooling during solidification, inducing the formation of AlFeCr particles having a polygonal morphology. This behavior has been attributed to the lower solubility of Cr in the α-Al matrix when compared to the

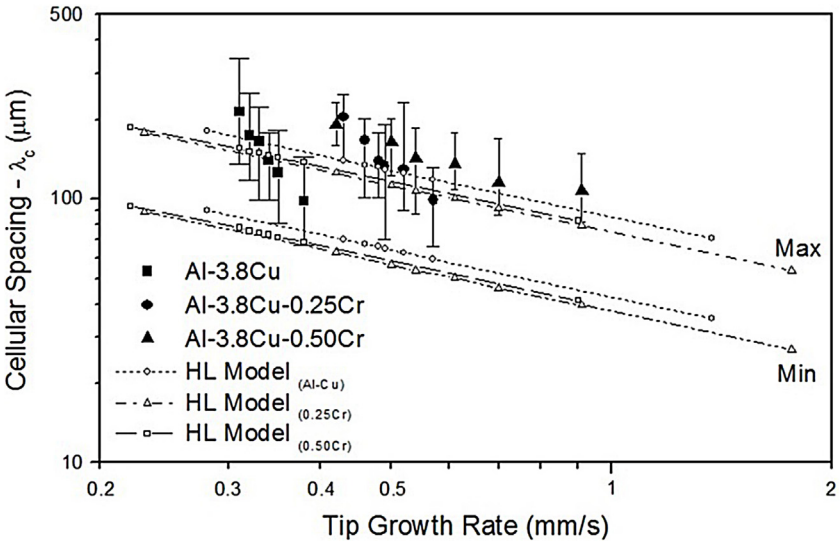

Fig. 5 – Comparison between experimental and theoretical cellular spacings as a function of tip growth rate and solidification cooling rate. R^2: coefficient of determination.

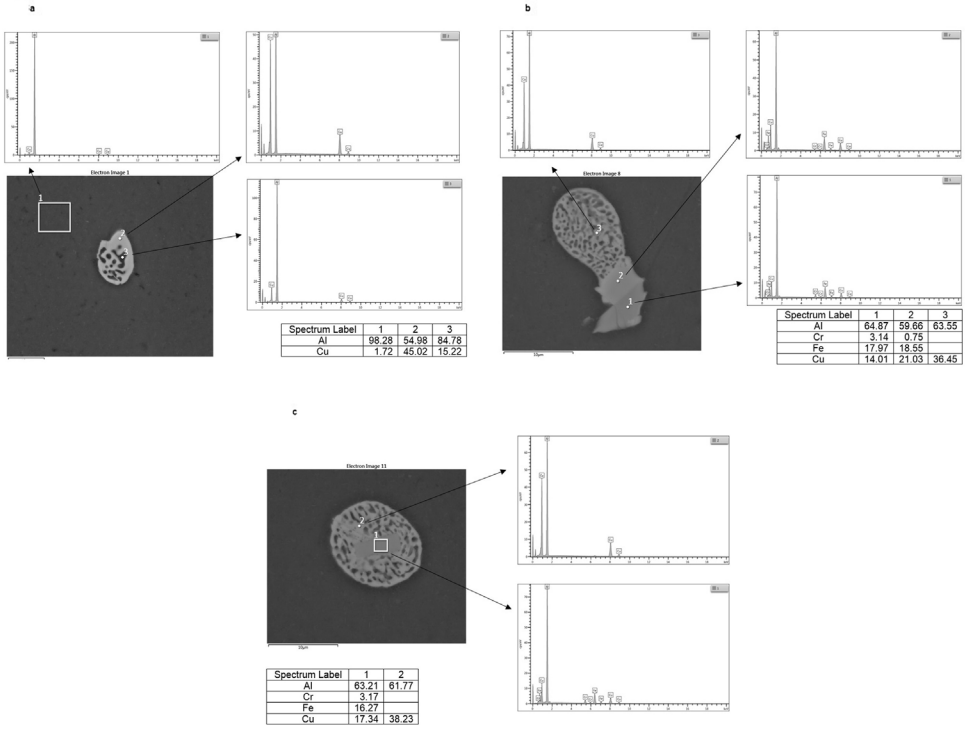

Fig. 6 – SEM micrographs and EDS analyzes for the Al–3.8Cu–0.25Cr alloy: (a) α-Al matrix and eutectic mixture, (b,c) eutectic mixture and AlCuCrFe precipitates.

solubility in the Al–Fe intermetallics. They have also stated that the formation of AlCr may be suppressed with small Cr addition. Similar behavior was observed by Aranda et al. [30] for Al–Si–Fe alloys with different Cr contents (1%, 3% and 5%). The presence of Cr decreased the formation of the Al_3FeSi_2 intermetallic compound, and a complex AlSiFeCr intermetallics was observed to occur as well as an additional σ-CrFe phase. They have concluded that the addition of Cr prevents the formation of isolated Al–Fe intermetallic particles in Al-based alloys with Fe concentrations.

With the addition of 0.5Cr the microstructure morphologies shown in Fig. 7 present an α-Al matrix with Cu in solid solution (EDS 1 – Fig. 7a) and a eutectic mixture of $CuAl_2$ and α-Al (EDS 2 – Fig. 7b and EDS3 – Fig. 7c), similar to the alloy having 0.25Cr. The incidence of isolated irregular AlCuCrFe precipitates was detected, in some situations with different colorations (EDS 1 and 2 – Fig. 7b and c). EDS analyzes suggested that these aspects result from different chemical compositions of each precipitate. The dark gray precipitate presented elemental chemical compositions of Al (~63%), Cr

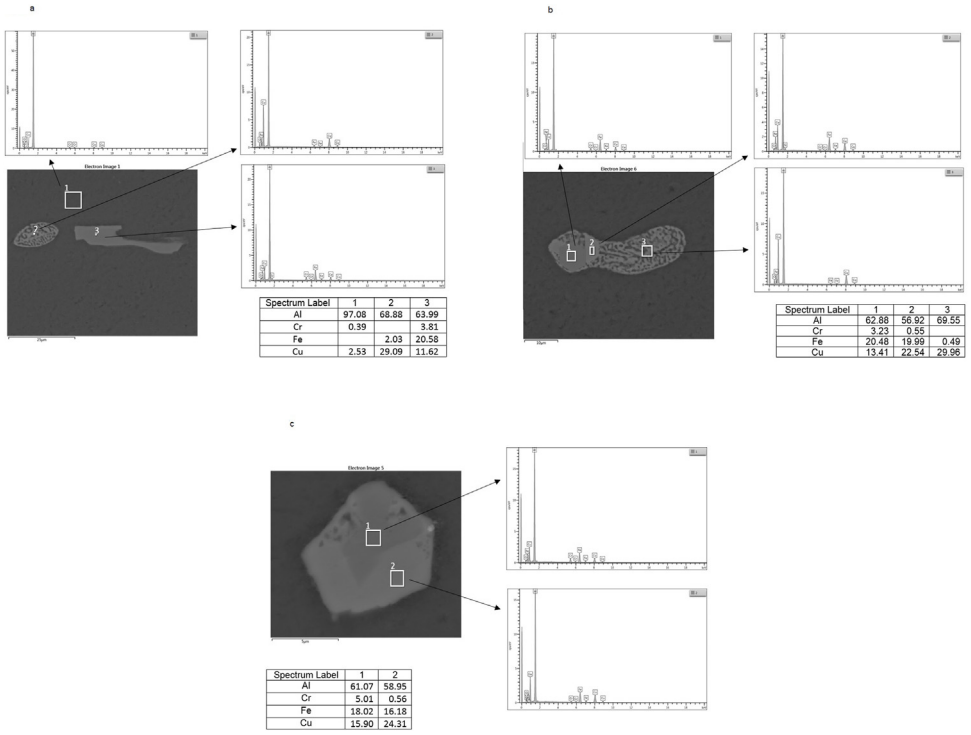

Fig. 7 – SEM micrographs and EDS analyzes for the Al–3.8Cu–0.50Cr alloy: (a) eutectic mixture and AlCuCrFe precipitates, (b) α-Al matrix, eutectic mixture and AlCuCrFe precipitate, (c) AlCuCrFe precipitates.

(~3–5%), Fe (~18–20%) and Cu (~11–16%), whereas the light gray indicated the presence of Al(~58%), Cr (~0.5–0.76), Fe (~16–19%) and Cu (~22–24%). The dark precipitate showed higher Cr and lower Cu contents while Fe concentration was practically identical in both precipitates. Moreover, needle-like Al-Fe binary particles are absent in all samples, evidencing that the Fe concentration of the investigated alloys is insufficient to precipitate this type of intermetallic compound. Similar results were obtained by Ravikumar et al. [31] with Al–4.5Cu based-alloys with Cr additions of 0.1,1 and 2 wt% and a percentage of 0.1Fe. Ezemenaka et al. [32] investigated the Al-rich corner of the Al-Cr-Fe system, reporting that the $Al_{13}Fe_4$ binary phase can be formed in the α-Al + AlFe eutectic mixture even when the Fe content is lower than 0.02 wt%. However, as the Cr solubility in the AlFe phase is higher than in the α-Al matrix, the tendency to form AlCrFe ternary compounds may suppress the formation of AlFe.

XRD analyzes were carried out to confirm the microstructures observed by SEM–EDS. Fig. 8 shows X-ray diffraction patterns of the alloys. For the binary Al–3.8Cu alloy, the identified phases were α-Al (FCC) and θ-$CuAl_2$ (tetragonal), typical hypoeutectic Al–Cu microstructures. Weak peaks at 2θ values of 12.5°, 22°, 24° and 31° were detected in the spectrum corresponding to the $Al_{13}Fe_4$ (orthorhombic) intermetallic compound. With 0.25Cr and 0.50Cr addition, X-ray spectrograms showed two peaks at around 40.5° and 42.5°, identified as $Al_7CrCuFe$ (orthorhombic) and $Al_{23}CuFe$ (orthorhombic) intermetallic compounds, respectively. Binary AlCr and AlFe compounds were undetected possibly due to higher Cr tendency to combine with Fe and higher cooling rates that minimize solute redistribution during solidification.

Quantitative phase analyzis resulting from the X-ray diffraction analyzes are presented in Table 3. For the Al–3.8Cu alloy, the presence of the $Al_{13}Fe_4$ compound was observed at positions nearest the top of the ingots due to solute segregation during solidification. With the increase in the alloy Cr content, the amount of α-Al decreases, the quantity of $Al_{23}CuFe_4$ and $Al_7CrCuFe$ increases and the $Al_{13}Fe_4$ compound was undetected. Lattice parameters of the α-Al and θ-$CuAl_2$ phases were obtained using the Rietveld method with Diffract Eva diffraction software and the values were identical for all alloys investigated in this work, as well as for all positions along the length of the ingots. The last column in Table 3 shows the sum of $Al_{23}CuFe_4$ and $Al_7CrCuFe$ phases. The values are similar to those reported in the literature for Al-Cu alloys with small additions of Cr and Fe [11,33,34]. The observed α-Al lattice parameter (4.030 Å) is different than that of pure Al (4.049 Å) due to the Al(rich)-Cu solid solution formation. Since the Cu atomic radius (1.28 Å) is lower than that of Al (1.43 Å), at dissolution of Cu in the α-Al phase lattice volume reduces. According to Draissia and Debili [35] the α-Al phase lattice parameter of 4.030 Å corresponds to the Cu solubility in Al in the range of 3.96–4.97 wt.%. Here we proposed that Cr and Fe in the investigated range practically did not impact such crystallographic parameters due to their small contents of the investigated alloys. It is well known that high solidification cooling rates (non-equilibrium conditions) have a strong influence on the solid formation. Aspects as the constitutional undercooling of the melt and the solidification interface instability directly affect microsegregation conditions and the extent of solid diffusion. Cooling rates higher than 10^4–10^6 (C/s achieved in some rapid-solidification processes result in

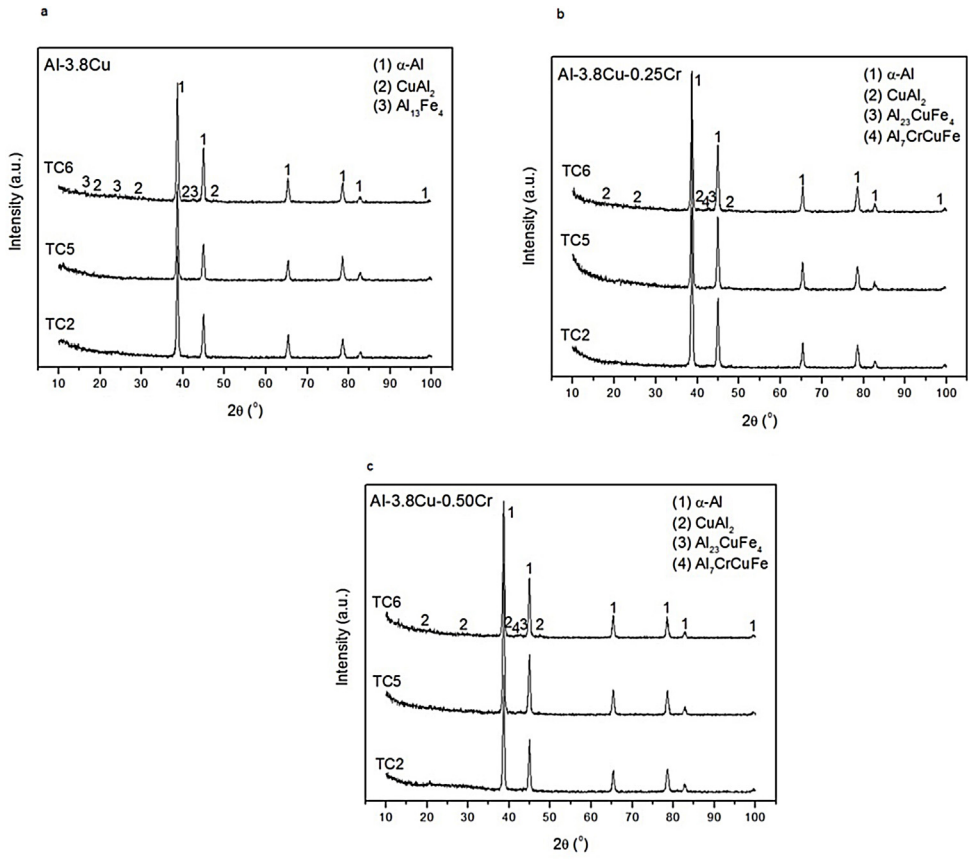

Fig. 8 – X-ray diffraction patterns of (a) Al–3.8Cu, (b) Al–3.8Cu–0.25Cr and (c) Al–3.8Cu–0.50Cr alloys at those positions corresponding to the TC2, TC5 and TC6 samples.

Table 3 – Results of X-ray diffraction analyzes.

	Crystal structure		Lattice parameter (Å)	
α-Al	(Cubic)		$a = 4.03$	
$CuAl_2$	(Tetragonal)		$a = 6.06$	$c = 4.87$
Quantity (%)				
Al–3.8Cu	α-Al	$CuAl_2$	$Al_{13}Fe_4$	$Al_{24}CuFe_4/Al_7CuCrFe$*
TC1	92.8	7.2	ND	ND
TC5	89.5	8.4	2.1	ND
TC6	90.1	5.1	4.8	ND
Al–3.8Cu–0.25Cr				
TC1	89.9	5.2	ND	4.8
TC5	89.3	6.3	ND	4.4
TC6	86.2	6.8	ND	6.8
Al–3.8Cu–0.50Cr				
TC1	84.1	10.0	ND	5.9
TC5	83.3	8.0	ND	8.7
TC6	83.5	8.6	ND	7.8

ND: not detected.

* This column shows the sum of $Al_{23}CuFe_4$ and $Al_7CrCuFe$ phases amount.

non-crystalline phases or non-equilibrium phase formation with solute trapping. However, in conventional solidification processes with cooling rates lower than 100 (C/s, the solute is rejected from the solid phase (if the partition coefficient is $k_0 < 1$) and accumulates in front of the solid–liquid interface, as a consequence of the solubility difference between the liquid and the solid phases. The effect of solidification cooling rate on the microsegregation has been studied in the last decades using both experimental and modeling approaches. Among the theoretical approaches indicated in [36], those proposed by Scheil (1942), Brody and Flemings (1966), Solari-Biloni (1980), Clyne-Kurz (1981), Ohnaka (1986),

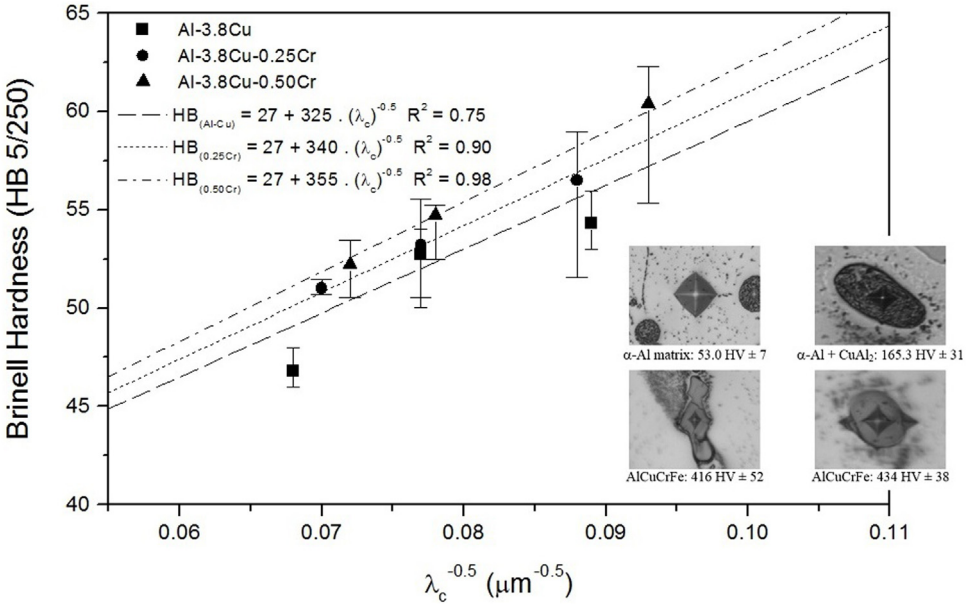

Fig. 9 – Hardness as a function of cellular spacing. R^2: coefficient of determination.

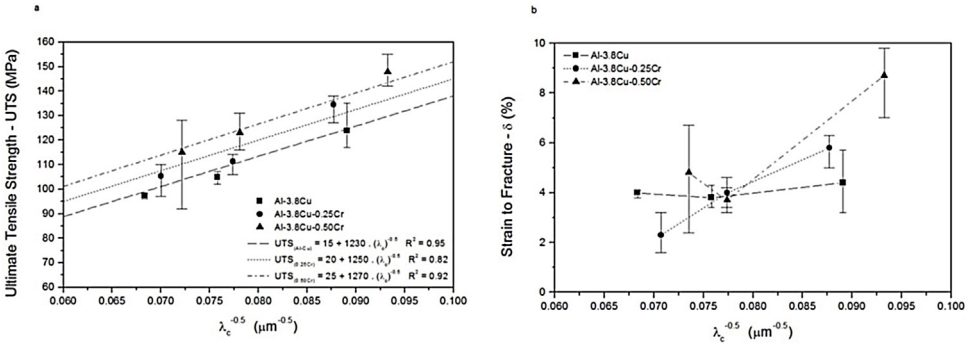

Fig. 10 – (a) Ultimate tensile strength and (b) strain to fracture as a function of cellular spacing. R^2: coefficient of determination.

Kobayashi (1988) and Battle-Pehlke (1990) are most significant.

3.3. *Hardness and tensile properties as a function of the length scale of the cellular microstructure*

Brinell hardness (HB) measured at 12, 30 and 50 mm from the bottom of the alloy's ingots are shown in Fig. 9. These locations are coincident with those from which tensile specimens were extracted. The results are average of six measurements for each position. Hardness results are presented using the formalism proposed by the Hall–Petch equation, that is, correlated to the reciprocal of the square root of λ_c. The Al–3.8Cu base alloy ingot showed a lower hardness profile along its length when compared to those of the Cr-containing alloys ingots. The position nearest the top of the ingots, i.e., highest λ_c (lowest $\lambda_c^{-0.5}$), presented the lowest HB. The addition of Cr increases the HB profiles of the 0.25Cr and 0.50Cr alloy ingots. The highest hardness was achieved in the Al–3.8Cu–0.50Cr alloy ingot at that position with the smallest λ_c (close to the cooled bottom of the ingot). When compared to the Al–3.8Cu alloy ingot, increase in hardness of 3.9% and 10% was observed at the position nearest the cooled bottom of the ingots with 0.25Cr and 0.50Cr additions, respectively. At positions closest to the top of the ingots the increase was 8.2% and 10.2% for the 0.25Cr and 0.50Cr alloys, respectively. The hardness dependence on Cr addition was evident, and its behavior was linear as a function of the reciprocal square root of λ_c. Several studies in the literature report the effect of higher Fe content on hardness of Al-based alloys [31,32,37–39]. However, the effects of lower Cr and Fe contents on hardness, is rarely reported. A study was conducted by Ravikumar et al. [31] in an Al–4.5Cu(wt%) alloy with additions of 0.1, 1 and 2 wt%Cr. According to the study, such Cr additions had no significant effect on hardness of the as-cast alloys, which presented values about 60HV, 62HV, 75HV and 77HV for 0, 0.1, 1 and 2 wt%Cr added, respectively. These values are similar to those found in the present work. Skoláková et al. [11] analyzed the hardness of high-alloyed Al–Cu–Fe alloys with contents of Cr and Ni in order to obtain quasicrystalline phases. They reported that the AlFe4Cu4Cr3 alloy in the as-cast condition presented hardness values

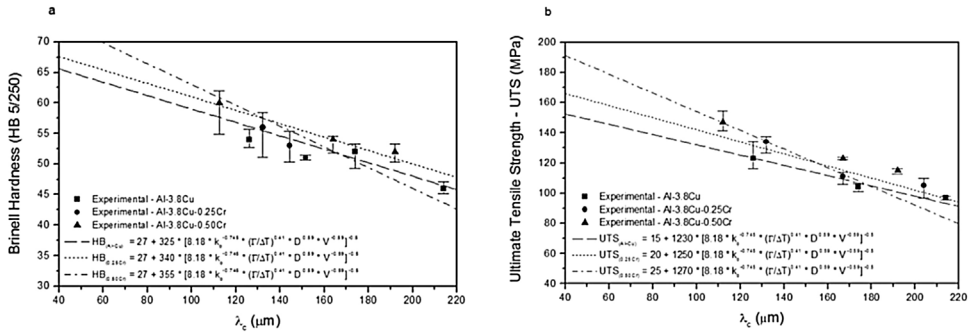

Fig. 11 – Comparison between experimental and theoretical: (a) hardness and (b) ultimate tensile strength as a function of cellular spacing.

around 80 HV due to the presence of intermetallic phases and quasicrystal structures. Vickers hardness measurements (HV 0.01 N) were also performed on both the matrix, eutectic mixture and precipitates. Fig. 9 presents indentation images and average values of nine measurements for each region. The α-Al matrix presented hardness values around 50 HV for all alloys, the eutectic mixture hardness about 165 HV and AlCuCrFe precipitates exhibited values higher than 400 HV.

Ultimate tensile strength (UTS) and strain to fracture (ε) results are shown in Fig. 10, and they represent average values of four specimens. Experimental equations are also displayed. According to these relations, the ultimate tensile strength increases with the increase in the alloy Cr content as well as with the decrease in λ_c (Fig. 10a). This is found by the increase in UTS profile of about 7.1% and 15.4% for the alloys ingots having 0.25Cr and 0.50Cr, respectively, as compared to the Al–3.8Cu alloy ingot along a same range of λ_c values. With respect to the strain to fracture (Fig. 10b), the Al–3.8Cu alloy exhibited almost constant values as a function of the cellular spacing, whereas alloys with Cr additions showed significant variation. For lower λ_c, the alloy containing 0.50Cr showed higher strain to fracture values despite its higher ultimate tensile strength, that is, showing an enhancement in toughness with Cr addition.

The experimental equations obtained in Figs. 9 and 10a were used to estimate hardness and ultimate tensile strength as a function of λ_c calculated by the Hunt–Lu model considering the upper limits for the spacings (Eq. (1)). Fig. 11 shows a comparison between theoretical and experimental results for HB and UTS. As observed, the theoretical values underestimated the cellular spacing, consequently the predicted HB (Fig. 11a) and UTS (Fig. 11b) were higher than the experimental data. These discrepancies were observed for all alloys. Similar behavior for cellular spacing in binary Sn–Pb and Al–Cu alloys have been reported in the literature [23–25,40], where the predictions by the Hunt–Lu model showed lower values than experimental data found under unsteady-state heat flow conditions and higher solidification cooling rates.

4. Conclusions

The following conclusions were extracted from the present investigation:

- The additions of 0.25Cr and 0.50Cr to the Al–3.8Cu base alloy permitted to refine the as-cast microstructure in terms of cellular spacing due to higher solidification cooling rates.
- When Cr was added to the binary Al–3.8Cu alloy, $Al_{23}CuFe$ and $Al_7CrCuFe$ intermetallic compounds were formed and Al–Fe intermetallic particles were unobserved, indicating that even low Cr addition prevented the formation of isolated Al-Fe compounds.
- The hardness and tensile strength were improved with the addition of Cr due to microstructure refining and precipitates formation. The experimental results allowed to obtain empirical equations relating the cellular spacing with both the solidification cooling rate and mechanical properties (hardness and ultimate tensile strength).
- The Hunt–Lu model was used to predict the cellular spacing. But the calculated results presented discrepancy with experimental observations for ternary Al–Cu–Cr alloys. When the model was coupled to the empirical equations for estimating hardness and ultimate tensile strength, the calculated values were overvalued.

Conflicts of interest

The authors declare no conflicts of interest

Acknowledgments

The authors acknowledge the support provided by CNPq (National Council for Scientific and Technological Development: grant: 403303/2016-8), FAPERGS (Fundação de Amparo à Pesquisa do Rio Grande do Sul), CAPES (Coordenação de Aperfeiçoamento de Pessoal de Nível Superior) and PUCRS (Pontifícia Universidade Católica do Rio Grande do Sul).

REFERENCES

[1] ASM Handbook. v. 2 – Properties and selection: nonferrous alloys and special-purpose materials. 10th ed Materials Park, Ohio: ASM International; 1990. p. 3470.
[2] Kaygısız Y, Maras N. Directional solidification of Al–Cu–Si–Mg quaternary eutectic alloy. J Alloys Compd 2017;721:764–71.
[3] Zuiko I, Kaibyshev R. Aging behavior of an Al–Cu–Mg alloy. J Alloys Compd 2018;759:108–19.

[4] Dorin T, Ramajayam M, Lamb J, Langan T. Effect of Sc and Zr additions on the microstructure/strength of Al–Cu binary alloys. Mater Sci Eng A 2017;707:58–64.
[5] Li H, Huang D, Kang W, Liu J, Ou Y, Li D. Effect of different aging processes on the microstructure and mechanical properties of a novel Al–Cu–Li alloy. J Mater Sci Technol 2016;32:1049–53.
[6] Raju PVK, Rajesh S, Rao JB, Bhargava NRMR. Tribological behavior of Al–Cu alloys and innovative Al–Cu metal matrix composite fabricated using stir-casting technique. Mater Today: Proc 2018;5:885–96.
[7] Chen TJ, Li XW, Guo HY, Hao Y. Microstructure and crystal growth direction of Al–Cu alloy. Trans Nonferr Metall Soc China 2015;25:1399–409.
[8] Zhao Y, Wang Z, Zhang C, Zhang W. Synchrotron X-ray tomography investigation of 3D morphologies of intermetallic phases and pores and their effect on the mechanical properties of cast Al–Cu alloys. J Alloys Compd 2019;777:1054–65.
[9] Mandal PK, Robi PS. Influence of micro-alloying with silver on microstructure and mechanical properties of Al–Cu alloy. Mater Sci Eng A 2018;722:99–111.
[10] Zhao M, Xing Y, Jia Z, Liu Q, Wu Z. Effects of heating rate on the hardness and microstructure of Al–Cu and Al–Cu–Zr–Ti–V alloys. J Alloys Compd 2016;686:312–7.
[11] Skoláková A, Novák P, Mejzlíková L, Salvetr P, Vojtech D. Structure and mechanical properties of Al–Cu–Fe–X alloys with excellent thermal stability. Materials 2017;10:1–19.
[12] Sugiyama K, Saito H, Hiraga K. On the crystal structures of the Al–Cu–Cr alloy system. J Alloys Compd 2002;324: 148–52.
[13] Sviridova TA, Schevchukov AP, Shelekhov EV, Diakonov DL, Tcherdyntsev VV, Kaloshkin SD. The quasicrystalline phase formation in Al–Cu–Cr alloys produced by mechanical alloying. J Alloys Compd 2011;509S:5299–303.
[14] Fu Y, Kang N, Liao H, Gao Y, Coddet C. An investigation on selective laser melting of Al–Cu–Fe–Cr quasicrystal: from single layer to multilayers. Intermetallics 2017;86:51–8.
[15] Salimon AL, Shevchukov AP, Stepashkin AA, Tcherdyntsev VV, Olifirov LK. Mechanical alloying as a solid state route for fabrication of Al–Cu–M(=Fe, Cr) quasicrystalline phases. J Alloys Compd 2017;707:315–20.
[16] Hunt JD, Lu SZ. Numerical modeling of cellular/dendritic array growth: spacing and structure predictions. Metall Mater Trans A 1996;27:611–23.
[17] ASTM International. ASTM E3-11(2017) standard guide for preparation of metallographic specimens. West Conshohocken, PA: ASTM International; 2017.
[18] ASTM International. ASTM E407-07(2015)e1 standard practice for microetching metals and alloys. West Conshohocken, PA: ASTM International; 2015.
[19] ASTM International. ASTM E92-17 Standard test methods for Vickers hardness and Knoop hardness of metallic materials. West Conshohocken, PA: ASTM International; 2017.
[20] ASTM International. ASTM E10-18 standard test method for Brinell hardness of metallic materials. West Conshohocken, PA: ASTM International; 2018.
[21] ASTM International. ASTM E8/E8M-16a standard test methods for tension testing of metallic materials. West Conshohocken, PA: ASTM International; 2016.
[22] Siqueira CA, Cheung N, Garcia A. Solidification thermal parameters affecting the columnar-to-equiaxed transition. Metall Mater Trans A 2001;33:2002–107.
[23] Rocha OL, Siqueira CA, Garcia A. Theoretical–experimental analysis of cellular and primary dendrite spacing during unidirectional solidification of Sn–Pb alloys. Mater Res 2002;5-3:391–7.
[24] Rocha OL, Siqueira CA, Garcia A. Cellular/dendritic transition during unsteady-state unidirectional solidification of Sn–Pb alloys. Mater Sci Eng A 2003;347:59–69.
[25] Rocha OL, Siqueira CA, Garcia A. Cellular spacings in unsteady-state directionally solidified Sn–Pb alloys. Mater Sci Eng A 2003;361:111–8.
[26] Rocha OL, Siqueira CA, Garcia A. Heat flow parameters affecting dendrite spacings during unsteady-state solidification of Sn–Pb and Al–Cu alloys. Metall Mater Trans A 2003;34:995–1006.
[27] Li J, Momono T. Effect of distribution coefficient ko on the structure of ultrasonic ingots during solidification of aluminium alloys. Mater Technol 2005;20(4):202–7.
[28] Kurtuldu G, Jessner P, Rappaz M. Peritectic reaction on the Al-rich side of Al–Cr system. J Alloys Compd 2015;621:283–6.
[29] Liu B, Yang XG, Huang HJ, Guo Z. The effect of alloying elements on the microstructure of Al–5Fe alloys. J Miner Metals Mater Soc 2012;64(2):316–22.
[30] Aranda VA, Figueroa IA, González G, García-Hinolosa JA, Lara-Rodríguez GA. Effect of small additions of Cr, Ti, and Mn on the microstructure and hardness of Al–Si–Fe–X alloys. Metals 2019;9(136):3–14.
[31] Ravikumar A, Sellamuthu R, Saravanan R. Effect of Cr addition on mechanical properties and wear rate of cast Al–Cu alloy. Indian J Sci Technol 2016;9(34):1–7.
[32] Ezemenaka D, Phiri A, Khvan A, Cheverikin V, fartushna I, Dinsdale A. An experimental investigation of phase transformation in the Al-rich corner of the Al–Cr–Fe system. J Alloys Compd 2019;808:1–10.
[33] Grushko B, Przepiórzynski B, Pavlyuchkov D, Mi S, Kowalska-Strzeciwilk E, Surowiec M. Complex intermetallics in Al–Cu–Cr system. J Alloys Compd 2007;442:114–6.
[34] Grushko B. A contribution to the Al–Cu–Cr phase diagram. J Alloys Compd 2017;729:426–37.
[35] Draissia M, Debili MY. Study of solid-solution hardening in binary aluminum-based alloys. Central Eur J Phys 2005;3(3):395–408.
[36] Meza ES, Bertelli F, Goulart PR, Cheung N, Garcia A. The effect of the growth rate on microsegregation: experimental investigation in hypoeutectic Al–Fe and Al–Cu alloys directionally solidified. J Alloys Compd 2013;561:193–200.
[37] Kaloshkin SD, Tcherdyntsev VV, Tomilin IA, Gunderov DV, Stolyarov VV, Baldokhin YV, et al. Composed phases and microhardness of aluminium-rich aluminium-iron alloys obtained by rapid quenching, mechanical alloying and high pressure torsion deformation. Mater Trans 2002;43(8):2031–8.
[38] Tcherdyntsev VV, Kaloshkin SD, Gunderov DV, Afonia EA, Brodova IG, Stolyarov VV, et al. Phase composition and microhardness of rapidly quenched Al–Fe alloys after high pressure torsion deformation. Mater Sci Eng A 2004;375–377:888–93.
[39] Baig M, Ammar HR, Seikh AH. Thermo-mechanical responses of nanocrystalline Al–Fe alloy processed using mechanical alloying and high frequency induction sintering. Mater Sci Eng A 2016;655:132–41.
[40] Spinelli JE, Cheung N, Garcia A. On array models theoretical predictions versus measurements for the growth of cells and dendrites in the transient solidification of binary alloys. Philos Magaz 2011;91(12):1705–23.